

Quantum electromechanics of a hypersonic crystal

Mahmoud Kalae^{1,2,4}, Mohammad Mirhosseini^{1,2,4}, Paul B. Dieterle^{1,2}, Matilda Peruzzo³, Johannes M. Fink^{2,3} and Oskar Painter^{1,2*}

Recent technical developments in the fields of quantum electromechanics and optomechanics have spawned nanoscale mechanical transducers with the sensitivity to measure mechanical displacements at the femtometre scale and the ability to convert electromagnetic signals at the single photon level. A key challenge in this field is obtaining strong coupling between motion and electromagnetic fields without adding additional decoherence. Here we present an electromechanical transducer that integrates a high-frequency (0.42 GHz) hypersonic phononic crystal with a superconducting microwave circuit. The use of a phononic bandgap crystal enables quantum-level transduction of hypersonic mechanical motion and concurrently eliminates decoherence caused by acoustic radiation. Devices with hypersonic mechanical frequencies provide a natural pathway for integration with Josephson junction quantum circuits, a leading quantum computing technology, and nanophotonic systems capable of optical networking and distributing quantum information.

Superconducting electromechanical circuits employing radiation pressure forces have recently been used to demonstrate sensitive measurement^{1–3} and control^{4–6} of mesoscopic mechanical objects in the quantum regime. The electromechanical coupling in these devices is typically achieved by a parametric interaction with a high-quality-factor (high-Q) electromagnetic resonator. In such interactions, the coupling is enhanced through the application of a strong electrical driving tone oscillating at a frequency that is equal to the difference between the resonance frequency of the mechanical mode and the typically much higher frequency of the electromagnetic resonator⁷. In the absence of a driving tone, the strength of the coupling at the quantum level is defined by a vacuum rate, g_0 , which for capacitively coupled circuits is related to the scale of the mechanical quantum zero-point motion in comparison to the dimension of the capacitor. Superconducting microwave resonators using nanoscale vacuum-gap capacitors can reach vacuum coupling levels of up to a few hundred hertz to megahertz-frequency mechanical oscillators⁸. These devices have been used for applications ranging from conversion between microwave and optical photons^{9–12} to the generation and detection of squeezed states of mechanical motion^{1–3}.

Similar work has sought to use radiation pressure to achieve parametric coupling to hypersonic (gigahertz or higher)¹³ mechanical oscillators. In the optical domain, this has been achieved in optomechanical crystals¹⁴, where reducing the optical mode volume to the nanoscale leads to large coupling between infrared photons and hypersonic phonons. Hypersonic acoustic devices are also being explored for their integration into superconducting quantum circuits^{5,15–23}. Towards this goal, piezoelectric materials^{24,25} can be used to reach MHz-rate electromechanical coupling^{12,19–23,26,27}; however, piezoelectric coupling cannot be turned off, nor is it perfectly mode selective, and polycrystalline piezoelectric materials can harbour lossy defects²⁸. Parametric radiation pressure coupling, on the other hand, can be dynamically controlled and is relatively insensitive to material properties, but is limited for

microwave electrical and hypersonic acoustical signals because of the mismatch in wavelengths.

Here we present an electromechanical crystal (EMC) structure that uses phononic crystals to engineer the localization and parametric coupling of mechanical motion. Using this concept, we demonstrate electromechanical coupling between an integrated high-impedance superconducting cavity and a mechanical mode at the hypersonic frequency of $\omega_m/2\pi = 0.425$ GHz. This EMC structure, akin to the optomechanical crystals, achieves a large photon-phonon coupling ($g_0/2\pi = 17.3$ Hz) through coherent addition of the coupling across multiple unit cells, and low acoustic damping ($\gamma/2\pi = 68$ Hz) by virtue of a phononic bandgap shield which eliminates acoustic radiation loss. A cooperative coupling between the electrical and acoustic modes of $C \approx 30$ is demonstrated, enabling transduction of hypersonic mechanical motion at the quantum level. Pushing from the ultrasonic into the hypersonic frequency range, EMC devices enter a new regime in parametric quantum acoustic transduction. In particular, they can be incorporated into phononic circuits as has been recently done with optomechanical systems^{12,29,30}. For chip-scale microwave-to-optical conversion, the hypersonic acoustic frequency of the EMC enables operation in the resolved sideband limit³¹, a critical parameter regime for realizing noise-free quantum signal conversion^{9,32}.

Electromechanical crystal design and fabrication

The electromechanical crystal studied in this work is formed from superconducting aluminium wiring on a patterned submicrometre-thick silicon membrane. The device consists of three primary elements: (1) a central nanobeam phononic crystal cavity and capacitor with nanoscale vacuum gap, (2) an acoustic shield with a phononic bandgap for all polarizations and propagation directions of acoustic waves, and (3) a nanoscale-pitch spiral coil inductor with minimal stray capacitance and large intrinsic impedance. Details of the planar spiral inductor are described in Supplementary Note 1. Here we focus on the design of the nanobeam cavity and acoustic shield. Figure 1a

¹Kavli Nanoscience Institute and Thomas J. Watson, Sr., Laboratory of Applied Physics, California Institute of Technology, Pasadena, CA, USA. ²Institute for Quantum Information and Matter, California Institute of Technology, Pasadena, CA, USA. ³Institute of Science and Technology Austria, Klosterneuburg, Austria. ⁴These authors contributed equally: Mahmoud Kalae, Mohammad Mirhosseini. *e-mail: opainter@caltech.edu

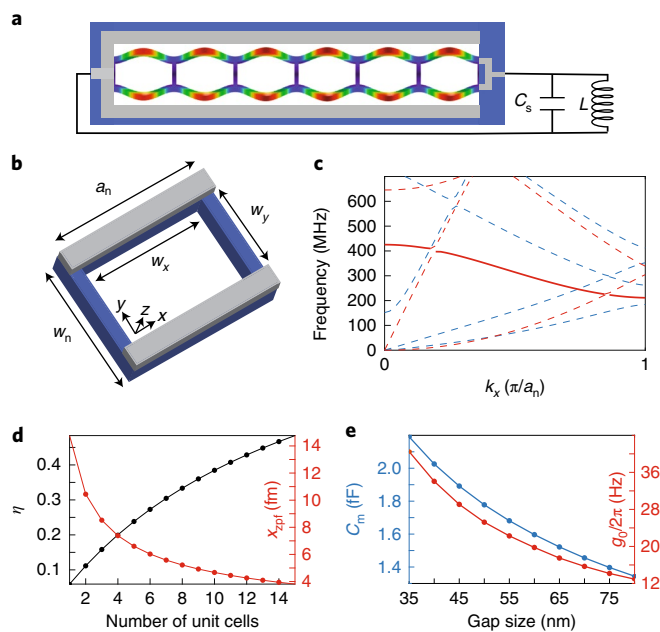


Fig. 1 | Nanobeam phononic crystal design. **a**, Schematic of the central nanobeam region showing the breathing mode. Mechanical motion is indicated by an exaggerated displacement of the beam structure, with red (blue) colour indicating regions of large (small) amplitude of the motion. The Al capacitor electrodes (grey) are connected in parallel to a coil inductor of inductance L and parasitic capacitance C_s . **b**, Unit cell of the nanobeam phononic crystal lattice with Si device layer (Al electrode) shown as blue (grey). **c**, Acoustic band structure (frequency versus wavenumber, k_x) for an infinitely periodic nanobeam phononic crystal with parameters $a_n = 1.55 \mu\text{m}$, $w_n = 900 \text{ nm}$, $w_x = 1.45 \mu\text{m}$ and $w_y = 600 \text{ nm}$. The Si device layer and Al electrode thicknesses are $t_{\text{Si}} = 220 \text{ nm}$ and $t_{\text{Al}} = 60 \text{ nm}$, respectively. The red and blue curves correspond to symmetric and antisymmetric modes with respect to the x - z symmetry plane. The band from which the breathing mode is formed is shown as a solid bold red curve. **d**, Participation ratio (η) and zero-point motion amplitude (x_{zpt}) of the breathing mode as a function of number of unit cells in the beam for a fixed parasitic capacitance $C_s = 3.1 \text{ fF}$ and a vacuum gap size of 45 nm . **e**, Motional capacitance, C_m , and zero-point coupling, g_0 , of the electrical circuit as a function of the gap size. Here the coil inductance, L , is adjusted for each gap to keep the LC resonance frequency fixed at $\omega_{\text{LC}} = 10.77 \text{ GHz}$. See Supplementary Notes 1 and 2 for details of mechanical and electrical numerical simulations.

depicts the patterned nanobeam cavity geometry and Al wiring layout of the vacuum-gap capacitor. The resulting hypersonic breathing acoustic cavity mode is also shown, visualized as an exaggerated deformation of the beam structure. Referring to the nanobeam unit cell and acoustic band structure of Fig. 1b, c, this breathing mode is formed from an acoustic band (solid bold red curve) near the Γ -point at wavevector $k_x = 0$. For a lattice constant of $a_n = 1.55 \mu\text{m}$, numerical finite-element method (FEM) simulations place the Γ -point frequency of the breathing mode band at $\omega_m/2\pi = 0.425 \text{ GHz}$.

Several subtle features of the nanobeam design are key to the realization of large electromechanical coupling g_0 (ref. 33). First, a minimum motional mass (m_{eff}) is desired to increase the zero-point amplitude $x_{zpt} = (\hbar/2m_{\text{eff}}\omega_m)^{1/2}$. In the case of the patterned nanobeam, this corresponds to minimizing both the thickness of the Si and Al layers and the width of the beam features. Second, a large motional capacitance (C_m) is desired, owing to limits on the achievable stray capacitance (C_s). The use of a Γ -point acoustic mode makes the electromechanical coupling from each unit cell additive, and thus increasing the number of unit cells in the acoustic

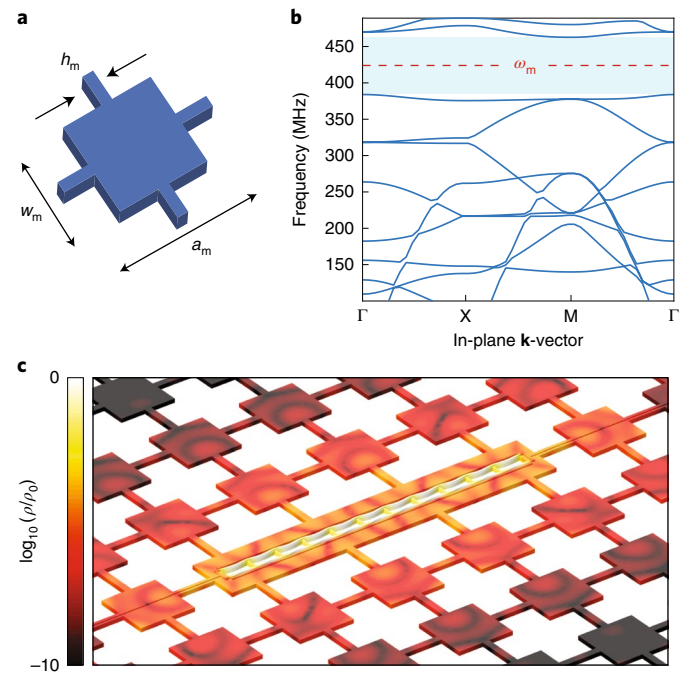


Fig. 2 | Phononic crystal shield. **a**, Schematic and dimensions of a unit cell in the phononic crystal shield (mirror cell) surrounding the nanobeam central cavity. **b**, Acoustic band structure of the acoustic shield for mirror unit-cell parameters $a_m = 5.13 \mu\text{m}$, $w_m = 2.1 \mu\text{m}$, $h_m = 360 \text{ nm}$, and a silicon layer thickness of $t_{\text{Si}} = 220 \text{ nm}$. The acoustic bandgap is shaded in blue, and the localized breathing mode frequency is marked with a dashed red line. **c**, Logarithmic scale colour plot of the acoustic energy density for the nanobeam breathing mode embedded in the acoustic shield of **a**. Acoustic energy density, ρ , is normalized to its peak value, ρ_0 , located in the nanobeam. Displacement of the structure is also used to visualize the breathing mode profile.

cavity results in an increased motional capacitance and participation ratio, $\eta = C_m/(C_m + C_s)$. FEM simulations of x_{zpt} and η versus the number of nanobeam unit cells are shown in Fig. 1d. Here, C_s is dominated by the stray capacitance of the planar spiral coil inductor forming the LC resonator. Figure 1e shows the resulting simulated vacuum coupling rate versus gap size of the breathing mode for a nanobeam structure consisting of 11 unit cells. Numerical simulations verify that extending the breathing mode of interest beyond this number of cells results in sensitivity to fabrication-induced disorder in the structure, leading to a series of localized resonances with reduced couplings.

The nanobeam phononic crystal does not have a full phononic bandgap in the vicinity of the breathing mode. To provide additional acoustic isolation from the surrounding Si membrane and substrate, the nanobeam cavity and vacuum-gap capacitor are embedded in the middle of a cross-pattern phononic bandgap crystal³⁴. A unit cell of the cross shield, shown in Fig. 2a, consists of a large square plate region with four narrow connecting tethers. The FEM-simulated acoustic band structure of an optimized cross structure (Fig. 2b) possesses a bandgap of nearly 0.1 GHz around the breathing mode at the frequency of 0.425 GHz. Using this optimized cross structure as an acoustic shield, we plot in Fig. 2c a simulation of the radiation pattern of the localized breathing mode when embedded in the phononic crystal. The energy density of the breathing mode is well confined, dropping by 100 dB within the first two periods of the shield.

A final design consideration relates to the high hypersonic frequency of the breathing mode. Coupling this mode to a microwave circuit of comparable frequency introduces a large effective detuning

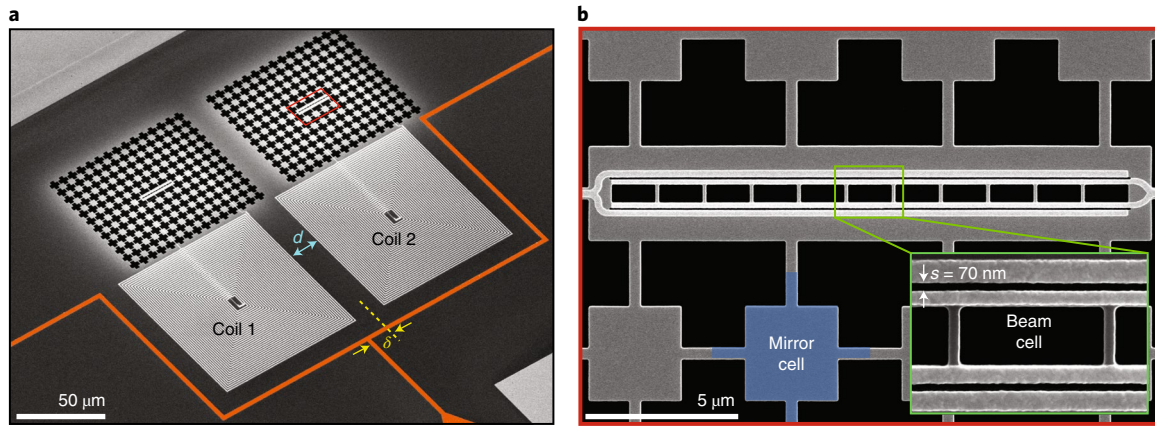


Fig. 3 | Fabricated structure. **a**, SEM image of the entire double-cavity device fabricated on a silicon-on-insulator membrane. The two Al spiral coils, labelled coil 1 and coil 2, are shunted via the vacuum-gap capacitor of two independent nanobeam acoustic cavities which are embedded inside acoustic shields. Inductive coupling between the two coils is set by the gap d . External coupling of the two coils to a 50- Ω microwave drive line is performed by shorting the end of a coplanar waveguide and splitting the current in the centre trace into two paths (shunting wire shown in orange). The offset δ from the centre of the coils where the wire path splits in two results in asymmetric coupling to the two coils, allowing for an adjustable amount of coupling between the even and odd supermodes of the coupled LC resonators. Parameters for this device are $d = 12 \mu\text{m}$ and $\delta = 16.5 \mu\text{m}$, resulting in a simulated coil coupling of $2J/2\pi = 415 \text{ MHz}$ and external coupling rates of $\kappa_{e,-}/2\pi = 9.6 \text{ MHz}$ ($\kappa_{e,+}/2\pi = 102 \text{ kHz}$) for the odd (even) mode. The bare (decoupled) frequency of the LC resonators is designed to be $\omega_{r,-}/2\pi = 10.86 \text{ GHz}$ for a capacitor vacuum gap of $s = 70 \text{ nm}$. **b**, Zoomed-in SEM image of the nanobeam phononic crystal region of the acoustic cavity coupled to coil 2. The Si electrode layer and Al electrodes appear dark and light grey, respectively. A mirror cell of the surrounding acoustic bandgap shield is shaded in blue. Inset: SEM of a unit cell of the nanobeam phononic cavity, indicating the $s = 70 \text{ nm}$ gap size.

in the parametric interaction, greatly increasing the required microwave pump power. We circumvent this problem by using a multimode microwave cavity³⁵ consisting of a pair of nearly degenerate single-mode LC resonators. The resonators are inductively coupled together with a coupling rate J , resulting in two hybridized supermodes consisting of a lower-frequency resonance at $\omega_{r,-}$ and an upper-frequency resonance at $\omega_{r,+} \approx \omega_{r,-} + 2J$. The lower- (upper-)frequency resonance is approximately an odd (even) superposition of the single-mode LC resonators. As detailed in Supplementary Note 3, for an acoustic mode (\hat{b}) directly coupled to just one of the single-mode LC resonators with vacuum coupling rate g_0 , and a microwave pump field applied near resonance with the odd-symmetry microwave supermode (\hat{a}_+), the resulting linearized electromechanical interaction Hamiltonian³¹ of the acoustic mode with the even-symmetry microwave supermode (\hat{a}_+) simplifies to $\hat{H}'_{em} = \hbar G (\hat{a}_+ \hat{b} + \hat{a}_+^\dagger \hat{b})$. Here, \hat{b} (\hat{b}^\dagger) and \hat{a}_+ (\hat{a}_+^\dagger) are annihilation (creation) operators for the acoustic and microwave modes, respectively, and G is a parametrically enhanced electromechanical coupling rate given by $G = g_{0,\pm} \sqrt{n_{d,-}}$, where $g_{0,\pm} = g_0/2$, and $n_{d,-}$ is the intra-cavity photon number in the odd supermode due to the applied pump field. In this scenario, efficient microwave pumping is realized for $2J \approx \omega_m$, corresponding to two-photon resonance where the microwave pump is at a drive frequency of $\omega_d = \omega_{r,+} - \omega_m \approx \omega_{r,-}$ (see Fig. 4c,d). The resulting electro-mechanical back-action scattering rate between microwave photons and acoustic phonons is $\gamma_{em} = 4G^2/\kappa_+$, where κ_+ is the decay rate of the even-symmetry cavity mode.

In Fig. 3a,b we show scanning electron microscope (SEM) images of a version of the double-cavity device fabricated using the process introduced in ref.³⁶. The two single-mode LC resonators are lumped element microwave resonators, each with a planar coil inductor which is used to couple them together through mutual inductance. To increase the device yield, we capacitively couple a hypersonic phononic crystal cavity to each of the single-mode LC resonators; however, being designed at slightly different (5 MHz) acoustic frequencies, they independently interact with the microwave supermodes of the system. Details of the fabrication are given in the Methods.

Electromechanical coupling and acoustic damping

We perform measurements of the EMC in a dilution refrigerator with a base temperature of $T_f = 10 \text{ mK}$ (Supplementary Note 4). As detailed in Fig. 3, microwave signals are launched onto a 50- Ω coplanar waveguide on the silicon-on-insulator (SOI) chip, and electrical excitation of the circuit is provided by inductive coupling to the two spiral inductors. We perform read-out of the electromechanical circuit response in reflection. Using a vector-network analyser, we plot in Fig. 4a,b microwave delay measurements of the device in Fig. 3, showing the presence of a heavily loaded low-Q resonance at $\omega_{r,-}/2\pi = 10.5788 \text{ GHz}$ and a more weakly coupled high-Q resonance at $\omega_{r,+}/2\pi = 10.9930 \text{ GHz}$. The measured splitting of $\Delta_{\pm}/2\pi = 414.2 \text{ MHz}$ is in close correspondence to the design tunnel-coupling rate of $2J/2\pi = 415 \text{ MHz}$. Fitting the measured delay curves to a Lorentzian lineshape, we infer a total damping rate of $\kappa_+/2\pi = 230 \text{ kHz}$ and an external coupling rate of $\kappa_{e,+}/2\pi = 85 \text{ kHz}$ for the microwave mode at $\omega_{r,+}$. For the more strongly loaded resonance at $\omega_{r,-}$, we measure $\kappa_-/2\pi \approx \kappa_{e,-}/2\pi = 8.9 \text{ MHz}$. Although the splitting and external coil coupling together indicate that the local modes of this device are strongly hybridized, more definitive evidence is provided by the measurement of the cross-mode electromechanical coupling $g_{0,\pm}$.

To probe the acoustic properties of the EMC, we use a two-tone pump and probe scheme^{43,38}, illustrated schematically in Fig. 4c. In this scheme, a strong drive tone (ω_d) is applied at a variable detuning from the lower-frequency microwave resonance, while a weaker probe tone (ω_p) is scanned across the upper-frequency microwave resonance. At two-photon resonance when the pump-probe difference frequency matches that of the acoustic mode ($\omega_p - \omega_d = \omega_m$), the beating of the drive and probe tones inside the cavity drives the acoustic mode. This leads to emergence of a transparency window in the reflected probe spectrum. In the weak-coupling, sideband-resolved limit the reflected probe spectrum is given by³⁸:

$$S_{11} = 1 - \frac{\kappa_{e,+}}{\frac{\kappa_+}{2} + i\delta_{r+p} + \frac{2G^2}{\gamma_+ + 2i(\delta_{r+p} - (\omega_m - \Delta_{r,d}))}} \quad (1)$$

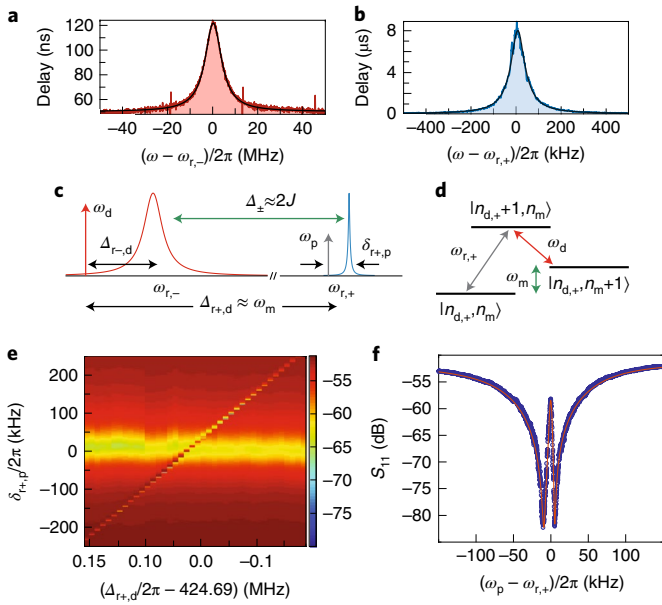


Fig. 4 | Microwave electromechanical spectroscopy. **a**, Vector-network analyser measurement of the time delay response of the lower-frequency, odd-symmetry-like microwave resonance centred at $\omega_{r,-}/2\pi = 10.5788$ MHz. **b**, Delay measurement of the higher-frequency, even-symmetry-like resonance centred at $\omega_{r,+}/2\pi = 10.9930$ MHz. **c**, Schematic showing the drive and probe frequencies and relevant LC resonance detunings used in the two-tone microwave spectroscopy measurements. Here, ω_d is the drive frequency, which is placed near the low-frequency LC resonance ($\omega_{r,-}$) and close to resonance with the lower motional sideband (red sideband) of the high-frequency LC resonance ($\omega_{r,+}$), and $\Delta_{r,d} \equiv \omega_{r,+} - \omega_d$. The high-frequency cavity response is registered by sweeping the frequency (ω_p) of the weak probe tone. **d**, Corresponding energy level diagram for red-detuned pumping scheme of **c**. $n_{d,+}$ is the intra-cavity photon number created by the drive tone in the high-frequency resonance, and n_m is the phonon occupation number in the mechanical mode. **e**, Colour plot of the measured normalized reflection spectrum, $|S_{11}|$, of a weak coherent probe tone as a function of the detuning ($\delta_{r,p} \equiv \omega_p - \omega_{r,+}$) from the upper-frequency resonance, and the detuning ($\Delta_{r,d}$) of the strong drive tone. **f**, Plot of the measured probe tone spectrum around the high-frequency LC resonance for a drive detuning at two-photon resonance, $\Delta_{r,d} \approx \omega_m = 2\pi \times 424.7$ MHz). The solid red curve is a fit to equation (1). In **e** and **f**, the strength of the drive tone corresponds to an intra-cavity photon number in the lower LC antisymmetric resonance of $n_{d,-} = 2.25 \times 10^5$.

where $\delta_{r,p} \equiv \omega_p - \omega_{r,+}$ and $\Delta_{r,d} \equiv \omega_{r,+} - \omega_d \approx \omega_m$. In Fig. 4e we plot a colour intensity map of a series of probe scans as the pump detuning is stepped in frequency, indicating the emergence of a dressed acoustic resonance near $\Delta_{r,d}/2\pi = 424.69$ MHz. A plot of the reflected probe spectrum for $\Delta_{r,d}/2\pi = \omega_m/2\pi = 424.7$ MHz and $n_{d,-} = 2.25 \times 10^5$ photons is shown in Fig. 4f. As was the case for roughly half of the tested devices, we did not find a second acoustic resonance on this device (see below for discussion). Fitting equation (1) to the measured probe spectrum, we find a total linewidth of $\gamma/2\pi = 6.8$ kHz for the acoustic mode. This linewidth contains contributions from electromechanical back-action (γ_{em}), intrinsic energy damping of the acoustic mode (γ_i) and any pure dephasing of the acoustic mode.

We implement a pair of time-domain measurements to determine directly the intrinsic acoustic damping and the electromechanical back-action (see Methods). In Fig. 5a we plot the measured ringdown of the acoustic mode energy as a function of the delay, δt , between the end of a ring-up pulse and the beginning of a read-out pulse

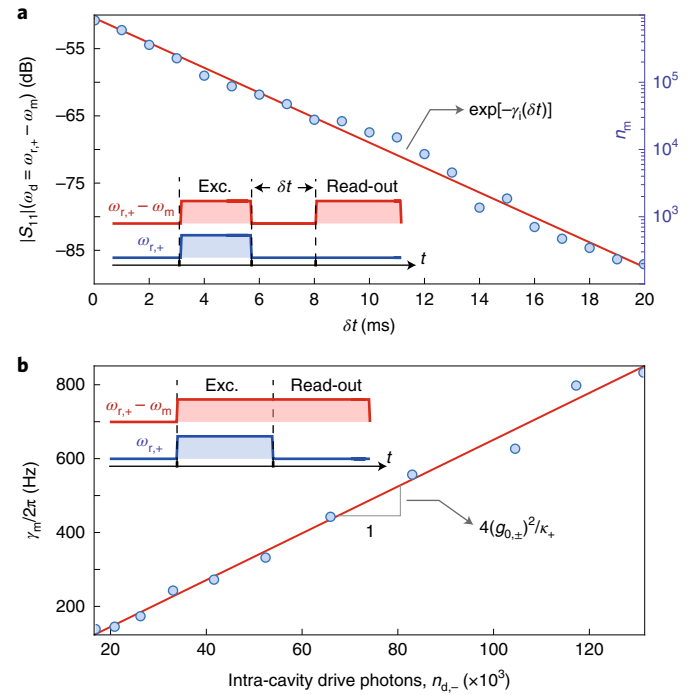


Fig. 5 | Mechanical ringdown and electromechanical coupling. **a**, Pulsed excitation and read-out measurement of the ringdown of the acoustic energy in the nanobeam resonator. Here ringdown occurs ‘in the dark’ with all microwave fields off. $|S_{11}|$ and n_m denote the amplitude of the reflected read-out pulse and the occupation number of the mechanical mode, respectively. Inset: ω_d , ω_m and $\omega_{r,+}$ denote the frequency of the strong drive tone, the resonance frequency of the mechanical mode and the resonance frequency of the even-symmetry cavity mode. **b**, The measured energy decay rate of the acoustic resonator, γ_{mv} , as a function of the power of the drive tone (see Supplementary Note 5). Here the drive tone is kept on after excitation, and the energy decay includes parametric back-action (and parasitic) damping due to the drive tone. The vacuum electromechanical coupling $g_{0,\pm}$ is extracted by fitting the measured decay rate γ_m versus the estimated intra-cavity photon number of the drive tone ($n_{d,-}$). κ_+ is the decay rate of the even-symmetry cavity mode.

(see inset). This ‘ringdown in the dark’ measurement yields the intrinsic energy damping rate of the mechanics, which for the breathing mode at $\omega_m/2\pi = 424.7$ MHz is measured to be $\gamma_i/2\pi = 68$ Hz (phonon lifetime $\tau = 2.3$ ms), corresponding to $Q = 6.25 \times 10^6$. We measure a series of such ringdown curves with the read-out pulse applied throughout the experiment. From these measurements, we are able to extract the back-action damped acoustic energy decay rate, $\gamma_m = \gamma_i + \gamma_{em}$, versus read-out pulse amplitude. The slope of the resulting plot, shown in Fig. 5b, yields a vacuum electromechanical coupling rate for the breathing mode of $g_{0,\pm}/2\pi = 17.3$ Hz (corresponding to $g_0/2\pi = 34.6$ Hz). Referring to Fig. 1d, this value is substantially larger than that expected for the vacuum-gap size of $s = 70$ nm measured by SEM at room temperature. We attribute this difference to a shrinking of the gap to $s \approx 40$ nm owing to an increase in the tensile strain of the Al wires on the nanobeam as the device is cooled to cryogenic temperatures. This is consistent with the observation that devices with gaps smaller than $s \leq 60$ nm at room temperature ($\sim 25\%$) did not show any acoustic resonances when cooled down, probably owing to a closing of the gap.

Frequency jitter and thermal occupancy

As quantified by the cooperativity, $C \equiv \gamma_{em}/\gamma_i$, and evidenced in the two-tone spectroscopy measurements of Fig. 4, coherent

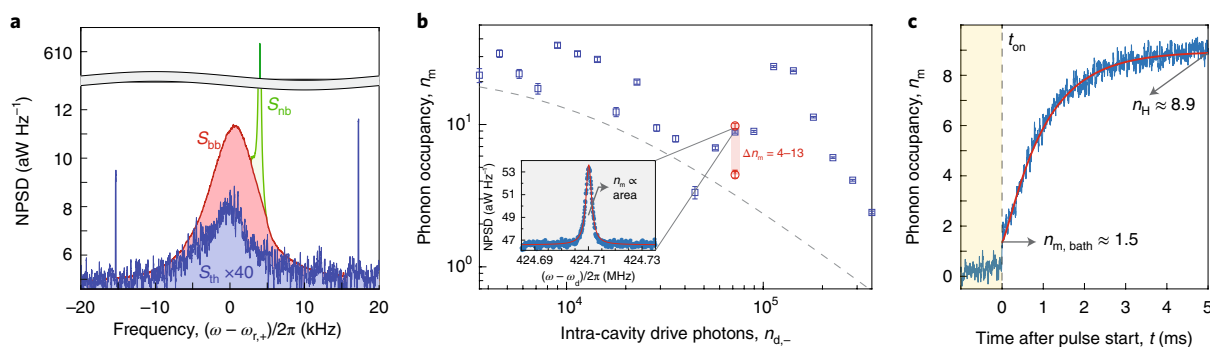


Fig. 6 | Frequency jitter noise and mode occupancy. **a**, Electrical noise power spectral density (NPSD) measured at the upper LC resonance ($\omega_{r,+}$) under red-detuned pumping with drive frequency $\Delta_{r,+d} \approx \omega_m$ and intra-cavity drive photon number $n_{d,-} = 4.3 \times 10^5$, with and without an additional weak tone at $\omega_{r,+}/2\pi + 4$ kHz. With the weak tone off, the measured noise power spectral density is just that of the back-action damped acoustic resonance (S_{bb} ; blue curve, magnified $\times 40$). With the weak tone on, the measured noise spectrum can be separated into two distinct components, a broad thermal-like spectrum S_{bb} (red curve) and a narrow noise peak around the weak coherent tone S_{nb} (green curve). **b**, Back-action cooling curve showing measured phonon occupancy versus drive tone power for a pump frequency $\Delta_{r,+d} \approx \omega_m$. For comparison purposes, the dashed grey curve corresponds to the theoretical back-action cooling curve for a fixed bath temperature of $T_b = 500$ mK and intrinsic mechanical damping rate $\gamma_i/2\pi = 68$ Hz. $n_{d,-} = 1$ corresponds to $P_{in} = 0.62$ fW at the input to the circuit. Inset: measured noise power spectral density at a drive power of $n_{d,-} = 7.1 \times 10^4$. Error bars in phonon occupancy correspond to 90% confidence interval in fit to area under Lorentzian noise power spectral density. **c**, Calibrated noise power in units of breathing mode phonon number, n_m , versus time during a red-detuned ($\omega_d = \omega_{r,+} - \omega_m$) drive pulse. Here a pulse train with pulse period $T_{per} = 30$ ms and on-pulse length $T_{on} = 15$ ms is used. t_{on} marks the instance of time when the drive tone is switched on. Pulse amplitude corresponds to an intra-cavity drive photon number $n_{d,-} = 7.1 \times 10^4$. The solid red curve shows a heating model fit to the data (see Supplementary Note 8) with the initial bath occupancy $n_{m,bath} = 1.5$ and a pump-induced hot bath occupancy $n_H = 8.9$. The overall phonon occupancy scale in **b**, **c** has a systematic uncertainty of 17% due to uncertainty in the measured γ_{em} and the gain in the microwave amplifier chain.

manipulation of the breathing mode via microwave drive fields is possible. A maximum cooperativity of $C \approx 30$ is obtained in this work at the highest attainable drive power of $n_{d,+} = 4.3 \times 10^5$ (see Supplementary Note 6). For quantum applications, one is also interested in the quantum cooperativity, defined as $C_{eff} \equiv C/n_b$, where n_b is a noise occupancy (Bose factor) of the bath coupled to the acoustic mode. $C_{eff} > 1$ allows for coherent manipulations of the mechanics on a timescale faster than decoherence caused by the bath, or in terms of dissipative processes, back-action cooling of the mechanical mode to its quantum ground state. We explore here the noise baths coupled to the EMC by monitoring the noise power spectrum generated on the upper motional sideband of a pump tone at $\omega_d = \omega_{r,+} - \omega_m$.

We plot in Fig. 6a the measured noise power spectral density around $\omega_{r,+}$. In this plot, the blue-shaded spectrum labelled S_{bb} is the back-action damped noise spectrum of the breathing mode, magnified by a factor of 40 for visibility. The linewidth of this spectrum is 6.7 kHz, substantially larger than the estimated linewidth from back-action and intrinsic damping alone ($[\gamma_i + \gamma_{em}]/2\pi \approx 2$ kHz). This broadening of the mechanical spectrum is due to time-averaging of the aforementioned frequency jitter. An estimate of the timescale of the jitter noise can be determined using the method described in refs.^{39,40}, in which a weak coherent tone is applied close to the upper motional sideband. We show in Fig. 6a the resulting measured noise power spectral density using this technique. The spectrum is separated into a broad thermal-like spectrum (S_{bb} ; red curve) and a narrower spectrum around the applied coherent tone (S_{nb} ; green curve). Acoustic frequency fluctuations faster than the instantaneous linewidth (given by $\gamma_i + \gamma_{em}$) contribute to S_{bb} whereas lower frequency fluctuations add to the narrow spectrum S_{nb} . We estimate that 15% (58%) of the measured total linewidth is a result of fast (slow) frequency jitter noise.

By calibrating the reflected signal amplification, we can also relate the area under the noise power spectral density S_{bb} to an estimate of the noise phonon occupancy of the breathing mode, n_m (ref.³¹). A plot of the inferred n_m versus drive photon number $n_{d,-}$ is shown in Fig. 6b. Although significant back-action cooling⁴¹ is expected based upon the measured cooperativity, the variation in n_m versus

drive power is highly irregular. The breathing mode starts out hot at low power, following a weak cooling trend with large fluctuations between different drive powers. Repeated measurement of n_m at a single drive power also show fluctuations (see red data points at $n_{d,-} = 7.1 \times 10^4$ in Fig. 6b). To confirm that the breathing mode is thermalized close to the fridge temperature in the absence of microwave driving of the circuit, we plot in Fig. 6c the total measured acoustic noise power versus time as the red-sideband cooling pump tone is switched on (see Methods). The breathing mode occupancy at the onset of the pulse is $n_m = 1.5$ (mode temperature $T_m \approx 40$ mK) and then heats over several milliseconds up to an occupancy $n_H = 8.9$. Over a train of pulses we observe n_H to fluctuate on timescales of a few seconds to minutes, with a variance consistent with the continuous-wave mode occupancy measurements. See Supplementary Note 7 for further discussion of the frequency jitter and anomalous mechanical heating measured in the current devices.

Conclusions

In conclusion, we present the design concept of an electromechanical crystal structure and experimentally realize it to demonstrate coupling between a multimode superconducting microwave cavity and a hypersonic phononic crystal oscillator. Device fabrication is performed using an Al-on-SOI materials platform compatible with both silicon photonics and superconducting qubits^{36,42}. The design of the acoustic cavity uses a phononic crystal to enable efficient coupling to a single mode at frequency $\omega_m/2\pi = 0.425$ GHz. A phononic bandgap shielding further reduces the coupling of the acoustic mode to external modes of the substrate, resulting in a measured intrinsic Q of 6.25×10^6 , 600 times as large as can be obtained for a device without a shield. A cooperative coupling between the microwave electrical circuit and the hypersonic acoustic mode of $C \approx 30$ is achieved, enabling sensitive electrical measurement of the acoustic mode close to its quantum ground state (mode occupancy $n_m = 1.5$).

The use of a different superconducting material with short quasi-particle relaxation time and a clean surface—such as NbTiN (ref.⁴³) may reduce acoustic mode heating and frequency jitter. Improvements in circuit design can also help to further increase the

back-action rate, operational bandwidth and the acoustic frequency of the EMC studied here. Using a parametric pump tone near d.c.^{5,44}, effectively replacing the lower-frequency microwave resonance of the current devices, can greatly reduce the heating caused by absorption of drive photons. A simple scaling of the device used here indicates that for an applied bias of 10 V, electromechanical coupling at the MHz level should be possible for acoustic modes at frequencies up to several GHz.

Online content

Any methods, additional references, Nature Research reporting summaries, source data, statements of data availability and associated accession codes are available at <https://doi.org/10.1038/s41565-019-0377-2>.

Received: 14 August 2018; Accepted: 15 January 2019;

Published online: 18 February 2019

References

- Wollman, E. E. et al. Quantum squeezing of motion in a mechanical resonator. *Science* **349**, 952–955 (2015).
- Pirkkalainen, J. M., Damskäg, E., Brandt, M., Massel, F. & Sillanpää, M. A. Squeezing of quantum noise of motion in a micromechanical resonator. *Phys. Rev. Lett.* **115**, 243601 (2015).
- Lecocq, F., Clark, J. B., Simmonds, R. W., Aumentado, J. & Teufel, J. D. Quantum nondemolition measurement of a nonclassical state of a massive object. *Phys. Rev. X* **5**, 041037 (2015).
- Teufel, J. D. et al. Circuit cavity electromechanics in the strong-coupling regime. *Nature* **471**, 204–208 (2011).
- Pirkkalainen, J.-M. et al. Hybrid circuit cavity quantum electrodynamics with a micromechanical resonator. *Nature* **494**, 211–215 (2013).
- Palomaki, T. A., Harlow, J. W., Teufel, J. D., Simmonds, R. W. & Lehnert, K. W. Coherent state transfer between itinerant microwave fields and a mechanical oscillator. *Nature* **495**, 210–214 (2013).
- Teufel, J. D. et al. Sideband cooling of micromechanical motion to the quantum ground state. *Nature* **475**, 359–363 (2011).
- Teufel, J. D., Donner, T., Castellanos-Beltran, M. A., Harlow, J. W. & Lehnert, K. W. Nanomechanical motion measured with an imprecision below that at the standard quantum limit. *Nat. Nanotechnol.* **4**, 820–823 (2009).
- Safavi-Naeini, A. H. & Painter, O. Proposal for an optomechanical traveling wave phonon–photon translator. *New J. Phys.* **13**, 013017 (2011).
- Andrews, R. W. et al. Bidirectional and efficient conversion between microwave and optical light. *Nat. Phys.* **10**, 321–326 (2014).
- Bochmann, J., Vainsencher, A., Awschalom, D. D. & Cleland, A. N. Nanomechanical coupling between microwave and optical photons. *Nat. Phys.* **9**, 712–716 (2013).
- Balram, K. C., Davanco, M. I., Song, J. D. & Srinivasan, K. Coherent coupling between radiofrequency, optical and acoustic waves in piezo-optomechanical circuits. *Nat. Photon.* **10**, 346–352 (2016).
- Maldovan, M. Sound and heat revolutions in phononics. *Nature* **503**, 209–217 (2013).
- Eichenfield, M., Chan, J., Camacho, R. M., Vahala, K. J. & Painter, O. Optomechanical crystals. *Nature* **462**, 78–82 (2009).
- Schoelkopf, R. J. & Girvin, S. M. Wiring up quantum systems. *Nature* **451**, 664 (2008).
- LaHaye, M. D., Suh, J., Echternach, P. M., Schwab, K. C. & Roukes, M. L. Nanomechanical measurements of a superconducting qubit. *Nature* **459**, 960–964 (2009).
- O’Connell, A. D. et al. Quantum ground state and single-phonon control of a mechanical resonator. *Nature* **464**, 697 (2010).
- Gustafsson, M. V. et al. Propagating phonons coupled to an artificial atom. *Science* **346**, 207–211 (2014).
- Chu, Y. et al. Quantum acoustics with superconducting qubits. *Science* **358**, 199–202 (2017).
- Manenti, R. et al. Circuit quantum acoustodynamics with surface acoustic waves. *Nat. Commun.* **8**, 975 (2017).
- Satzinger, K. J. et al. Quantum control of surface acoustic wave phonons. *Nature* **563**, 661–665 (2018).
- Moores, B. A., Sletten, L. R., Viennot, J. J. & Lehnert, K. Cavity quantum acoustic device in the multimode strong coupling regime. *Phys. Rev. Lett.* **120**, 227701 (2018).
- Arrangoiz-Arriola, P. et al. Coupling a superconducting quantum circuit to a phononic crystal defect cavity. *Phys. Rev. X* **8**, 031007 (2018).
- Eom, C.-B. & Trolier-McKinstry, S. Thin-film piezoelectric mems. *MRS Bull.* **37**, 1007–1017 (2012).
- Piazza, G., Felmetsger, V., Murali, P., Olsson, R. H.III. & Ruby, R. Piezoelectric aluminum nitride thin films for microelectromechanical systems. *MRS Bull.* **37**, 1051–1061 (2012).
- Han, X., Zou, C.-L. & Tang, H. X. Multimode strong coupling in superconducting cavity piezoelectromechanics. *Phys. Rev. Lett.* **117**, 123603 (2016).
- Arrangoiz-Arriola, P. & Safavi-Naeini, A. Engineering interactions between superconducting qubits and phononic nanostructures. *Phys. Rev. A* **94**, 063864 (2016).
- Phillips, W. A. Tunneling states in amorphous solids. *J. Low Temp. Phys.* **7**, 351–360 (1972).
- Fang, K., Matheny, M. H., Luan, X. & Painter, O. Optical transduction and routing of microwave phonons in cavity-optomechanical circuits. *Nat. Photon.* **10**, 489 (2016).
- Patel, R. N. et al. Single-mode phononic wire. *Phys. Rev. Lett.* **121**, 040501 (2018).
- Aspelmeyer, M., Kippenberg, T. J. & Marquardt, F. Cavity optomechanics. *Rev. Mod. Phys.* **86**, 1391–1452 (2014).
- Hill, J. T., Safavi-Naeini, A. H., Chan, J. & Painter, O. Coherent optical wavelength conversion via cavity optomechanics. *Nat. Commun.* **3**, 1196 (2012).
- Fink, J. M. et al. Quantum electromechanics on silicon nitride nanomembranes. *Nat. Commun.* **7**, 12396 (2016).
- Safavi-Naeini, A. H. & Painter, O. Design of optomechanical cavities and waveguides on a simultaneous bandgap phononic–photonic crystal slab. *Opt. Express* **18**, 14926–14943 (2010).
- Dobbrindt, J. M. & Kippenberg, T. J. Theoretical analysis of mechanical displacement measurement using a multiple cavity mode transducer. *Phys. Rev. Lett.* **104**, 033901 (2010).
- Dieterle, P. B., Kalae, M., Fink, J. M. & Painter, O. Superconducting cavity electromechanics on a silicon-on-insulator platform. *Phys. Rev. Appl.* **6**, 014013 (2016).
- Weis, S. et al. Optomechanically induced transparency. *Science* **330**, 1520–1523 (2010).
- Safavi-Naeini, A. H. et al. Electromagnetically induced transparency and slow light with optomechanics. *Nature* **472**, 69–73 (2011).
- Zhang, Y., Moser, J., Güttinger, J., Bachtold, A. & Dykman, M. I. Interplay of driving and frequency noise in the spectra of vibrational systems. *Phys. Rev. Lett.* **113**, 255502 (2014).
- Zhang, Y. & Dykman, M. I. Spectral effects of dispersive mode coupling in driven mesoscopic systems. *Phys. Rev. B* **92**, 165419 (2015).
- Marquardt, F., Chen, J. P., Clerk, A. A. & Girvin, S. M. Quantum theory of cavity-assisted sideband cooling of mechanical motion. *Phys. Rev. Lett.* **99**, 093902 (2007).
- Keller, A. J. et al. Al transmon qubits on silicon-on-insulator for quantum device integration. *Appl. Phys. Lett.* **111**, 042603 (2017).
- Barends, R. et al. Reduced frequency noise in superconducting resonators. *Appl. Phys. Lett.* **97**, 033507 (2010).
- Rouxinol, F. et al. Measurements of nanoresonator–qubit interactions in a hybrid quantum electromechanical system. *Nanotechnology* **27**, 364003 (2016).

Acknowledgements

This work was supported by the AFOSR MURI Wiring Quantum Networks with Mechanical Transducers (grant FA9550-15-1-0015), the ARO-LPS Cross-Quantum Technology Systems programme (grant W911NF-18-1-0103), the Institute for Quantum Information and Matter, an NSF Physics Frontiers Center (grant PHY-1125565) with support of the Gordon and Betty Moore Foundation, and the Kavli Nanoscience Institute at Caltech. M.M. acknowledges support from a KNI Postdoctoral Fellowship. J.M.F. acknowledges support from an IQIM Postdoctoral Fellowship.

Author contributions

M.K., J.M.F. and O.P. came up with the concept and planned the experiment. M.K., P.B.D., M.M., M.P., J.M.K. and O.P. designed and fabricated the device. M.K., M.M. and O.P. performed the measurements and analysed the data. All authors contributed to the writing of the manuscript.

Competing interests

The authors declare no competing interests.

Additional information

Supplementary information is available for this paper at <https://doi.org/10.1038/s41565-019-0377-2>.

Reprints and permissions information is available at www.nature.com/reprints.

Correspondence and requests for materials should be addressed to O.P.

Publisher’s note: Springer Nature remains neutral with regard to jurisdictional claims in published maps and institutional affiliations.

© The Author(s), under exclusive licence to Springer Nature Limited 2019

Methods

Device fabrication. The EMC device is fabricated using an Al-on-SOI process introduced in ref. ³⁶. The Al layer is deposited using electron-beam evaporation, and patterning of the Si membrane and Al wiring is performed using electron-beam lithography and a combination of plasma dry etching and lift-off (details described in the Supplementary Information). A SOI wafer with high resistivity ($\geq 5\text{ k}\Omega$) Si device and handle layers is used to reduce the microwave losses, and the buried-oxide (BOX) layer underlying the Si device layer is removed using an anhydrous hydrofluoric acid vapour etch to avoid Al etching and static friction (stiction) during the membrane release. Removal of the BOX layer is performed over an extended region covering the entire double-cavity structure in order to avoid the significant microwave losses in the BOX layer.

Ringdown time-domain measurements. We perform two types of ringdown measurements. In one, the mechanics is excited and freely decays ('ringdown in the dark'), and then its amplitude is read out. The other ringdown measurement is performed with the read-out signal on throughout the measurement, thus introducing back-action from the read-out signal on the mechanics during ringdown. In both scenarios, we apply a 100-ms two-tone pulse to ring up the mechanics with a strong drive tone at $\omega_d = \omega_{r,+} - \omega_m$ and a weak probe tone at $\omega_p = \omega_{r,+}$. The weak probe tone and drive tone are turned off at the end of the ring-up pulse. After a variable time delay the drive tone is pulsed back on for 15 ms. The scattered drive tone produces a read-out signal detected on a spectrum analyser which is set in zero-span mode with centre frequency at $\omega_{r,+}$ and resolution bandwidth (RBW) of 30 kHz ($\gg \gamma / 2\pi$). The acoustic mode occupancy is determined by the rate of scattered photons from the strong drive

tone within the first 25 μs of the measured read-out signal pulse. Plotting the measured read-out signal pulse amplitude versus time delay for a fixed power of the read-out drive tone pulse yields the intrinsic mechanical decay rate. To extract the back-action-induced damping rate of the breathing mode, the read-out pulse delay is set to $\delta t = 0$ and the motionally scattered photons within the read-out pulse are measured as a function of time throughout the ringdown of the mechanics. Fitting an exponential decay curve to the time-varying detected read-out signal on the spectrum analyser for varying powers of drive tone read-out yields the total acoustic decay including back-action from the read-out signal.

Thermal heating time-domain measurements. To measure the transient population dynamics of the hypersonic breathing mode in the presence of a red-sideband drive tone, we perform a time-domain measurement similar to that used to measure mechanical ringdown. Here a pulse train of red-detuned ($\omega_d = \omega_{r,+} - \omega_m$) drive tone pulses with pulse period $T_{\text{per}} = 30\text{ ms}$ and on-pulse length $T_{\text{on}} = 15\text{ ms}$ is applied to the EMC device. As shown in Fig. 6b, the motionally scattered drive tone produces a Lorentzian signal in the measured reflection spectrum centred around a frequency of $\omega_{r,+}$. Sending this signal into a spectrum analyser which is set in zero-span mode with centre frequency at $\omega_{r,+}$ and RBW = 30 kHz, one can measure the thermal mode occupancy with a time resolution of $1/(2\pi\text{RBW}) = 5\text{ }\mu\text{s}$. Averaging this signal over many pulses (10 hours) produces the heating curve shown in Fig. 6c.

Data availability

The data that support the findings of this study are available from the corresponding author (O.P.) upon reasonable request.